colorants

MDPI

Article

Effective Removal of Methyl Orange Dyes Using an Adsorbent Prepared from Porous Starch Aerogel and Organoclay

Rihem Jemai, Mohamed Amine Djebbi *, Saber Boubakri, Hafsia Ben Rhaiem and Abdesslem Ben Haj Amara

Laboratory of Ressources, Materials & Ecosystem (RME), Faculty of Sciences of Bizerte, University of Carthage, Zarzouna 7021, Tunisia

* Correspondence: med-djebbi@hotmail.fr or mohammed-amine.djebbi@inrae.fr; Tel.: +216-27-380-672

Abstract: Intending to provide efficient and compact wastewater remediation, the present work is exploiting and introducing a novel composite prepared from porous starch aerogel (PSA) and organically modified Ca-montmorillonite (OMMT) for the removal of dyes from aqueous samples. First, potato starch components were used as a hydrolysis precursor to obtain PSA. The organoclay samples were prepared by co-intercalation of octadecylamine (ODA) into Ca-MMT using a low-temperature melting procedure. Composites with different starch-to-organoclay ratios of 10:1, 1:1, and 1:10 were then prepared by a blending process in distilled water and used for methyl orange (MO) uptake. The removal of methyl orange dyes increased with the amount of organoclay in the PSA matrix. Characterization revealed that organoclay synergy improved the PSA surface chemistry, while an important improvement in textural properties and thermal stability was also observed. The composite's efficiency was demonstrated by high removal capabilities towards MO in most experimental runs, with a maximum adsorption capacity beyond 344.7 mg/g. The fitting result showed that MO adsorption follows a monolayer adsorption model, and chemisorption was the rate-controlling step. Nonetheless, this study proved the great potential of PSA/OMMT in dyeing wastewater treatment. Furthermore, starch modification is proven as an effective approach to enhancing the performance of starch-derived adsorbents.

Keywords: montmorillonite; porous starch; organoclay; methyl orange; adsorption; aerogel

Citation: Jemai, R.; Djebbi, M.A.; Boubakri, S.; Ben Rhaiem, H.; Ben Haj Amara, A. Effective Removal of Methyl Orange Dyes Using an Adsorbent Prepared from Porous Starch Aerogel and Organoclay. *Colorants* **2023**, *2*, 209–229. https://doi.org/10.3390/colorants2020014

Academic Editor: Anthony Harriman

Received: 6 March 2023
Revised: 10 April 2023
Accepted: 18 April 2023
Published: 1 May 2023

1. Introduction

Access to clean, safe, and reliable water is an essential requirement for the health and well-being of society, yet as societies continue to grow and affect the environment and ecosystems around them, clean water is becoming scarcer worldwide. As a result, water reuse has become an upcoming challenge in today's global resource management system. According to the latest statistics, approximately 300 million tons of synthetic compounds annually used in manufacturing sectors partially find their way into freshwater systems [1]. In particular, organic dyes are identified as the major contributors to water pollution caused by the discharge of effluent from various dye industries such as textile, leather, plastics, paper, printing, etc. [2–4]; almost 5000–10,000 tons of dyes are released into the waterways annually [5]. Methyl orange (MO) is among the very common water-soluble azo dyes that has been widely used in several dye industries since its inception [6]. This dye is highly hazardous due to its toxicity, deep color, oxygen depletion, and poor biodegradability [7,8]. When it is discharged directly into the water environment, we are seeing devastating effects on the aquatic ecosystem and the surrounding natural habitats. Increased cancer rates and other illnesses have been documented worldwide due to the accumulation of these toxic substances in the blood [3,9]. This, therefore, raises the urgency of finding proper methods for treating this organic dye from both industrial wastewater and polluted water bodies.

In recent years, much progress has been made in the development of appropriate strategies for wastewater treatment. For instance, flocculation, coagulation, adsorption,

filtration, chemical oxidation, membrane separation, photochemical degradation, and so forth have been applied [2,4,10,11]. Among them, adsorption is, nevertheless, the most convenient and well-established technique for dye removal from wastewater owing to its high efficiency, simplicity, low cost, and most importantly, its implementation in green environment planning [12–15]. Therefore, interest in lower-cost alternatives to high-availability sustainable biomass and minerals that would provide safe and economical methods of removing dyes from contaminated water has increased [16–19]. For this reason, the development of adsorbents from biorenewable polymers and clay minerals has been recognized as an ideal solution for wastewater treatment that minimizes waste, recovery, and reuse, and further aids the green goals [18,19]. To support the sustainable option for removing dyes, porous starch aerogel (PSA) and organoclay montmorillonite (OMMT) were introduced in this work and composited to obtain the PSA/OMMT composites using the process of aqueous gel precursor freezing, ethanol drying, low-temperature melting procedure, and aqueous dispersion.

Herein, porous starch-based polysaccharide components are derived from potato starch biomass. The main advantage of this biopolymer compared to other materials are associated with ease of availability, safe usage, low cost, biocompatibility, fast biodegradation rate, and amenability to modification [18–20]. Moreover, it contains several oxygen and hydroxyl functionalities due to its polymeric and branching structure. Although starch-based adsorbents have gained great interest in water purification owing to their outstanding properties, unmodified starch is rarely applied directly as an adsorbent for wastewater treatment because it also has some drawbacks, mainly due to its low surface area and limited thermal stability. Therefore, the incorporation of layered silicate organoclays montmorillonite in the porous starch matrix can improve its capacity to remove dyes from an aqueous solution and thus create a highly effective adsorbent. This is explained by the fact that the specific surface area increases as the polysaccharide-OMMT interactions are enhanced by exfoliating the organoclay, and the potential association of biopolymer chains through hydrogen bonds, which enhance the surface functionality of the composite [21,22]. Interestingly, previous research does present numerous studies of starchy matrices reinforced by MMT clays that address wastewater treatment and packaging applications [18,23–26]. However, to the best of our knowledge, no contribution is found for PSA/OMMT composites against MO dye molecules.

2. Experimental Methods

2.1. Materials

Potato starch powder ($(C_6H_{10}O_5)_n$) was purchased from Panreac Quimica SA (Barcelona, Spain). Wyoming-type montmorillonite, SWy-2, with a cation exchange capacity of 76.4 mequiv/100 g, supplied by the Clay Minerals Society, Crook County, Wyoming, was used for the experiment. The formula of the montmorillonite can be expressed as $(Ca^{2+}_{0.07}K^{+}_{0.01}Na^{+}_{0.20})[Al^{3+}_{1.53}Fe^{3+}_{0.18}Mg^{2+}_{0.26}Ti^{4+}_{0.01}][Si^{4+}_{3.96}Al^{3+}_{0.04}]$-$O_{10}(OH_2)$, as calculated from the chemical analyses. The crude clay was first Na-exchanged, then the secondary ion in the exchangeable position was Ca, and the resulting material was denoted as Ca-MMT. Sodium hydroxide (NaOH $\geq$ 98%), calcium chloride ($CaCl_2 \geq$ 97%), hydrochloric acid (HCl, 37%), ethanol (CH_3CH_2OH, 96.0%), octadecylamine ($CH_3(CH_2)_{17}NH_2 \geq$ 99%), and methyl orange ($C_{14}H_{14}N_3NaO_3S$, 85%), were analytical grade, purchased from Sigma-Aldrich, and used without further purification. All solutions were prepared in distilled water.

2.2. Preparation of PSA/OMMT Composites

The synthesis of PSA/OMMT composites was undertaken as follows (Figure 1): (i) Porous starch was prepared through the solvent exchange method [27,28]. Typically, 5 g potato starch powder was wholly dissolved in 100 mL distilled water and heated at 90 °C for 30 min to completely gelatinize the starch. Subsequently, the mixture was cooled (at 5 °C) and frozen in the refrigerator for 7 days until a starch gel was formed. The frozen starch was then immersed several times in 100 mL of ethanol for about 2 h each time to

remove ice, oven-dried at 50 °C for 3 h to remove excess ethanol, and finally white solid denoted as PSA was obtained. (ii) OMMT was synthesized by interaction (cation exchange) of Ca-MMT with octadecylamine (ODA) surfactant following the known low-temperature melting method [29]. Briefly, 20 g Ca-MMT was thoroughly soaked in 1 L of hot water (80 °C) with continuous stirring. Simultaneously, 7.7 g ODA and 2.9 mL of concentrated HCl were added to 500 mL of boiling water (80 °C) to obtain octadecylammonium cations. After that, this solution was poured into the hot clay water solution under vigorous stirring for 50 min until the clay was flocculated. The resulting precipitate was then filtered, washed thrice with hot water, and finally dried to yield the organoclay. (iii) Later, modification of porous starch was prepared according to the methodology prepared by Aouada et al. [30]. Shortly, different amounts of organoclay were preliminarily dispersed in distilled water (200 mL) using ultrasonication for 2 h. Next, they were separately added to the porous starch fraction and stirred for 3 h. Obtained products were finally placed in a vacuum-drying oven and dried at 80 °C overnight. The 3 composites were labeled PSA/OMMT according to the starch-to-organoclay ratios (10:1, 1:1, and 1:10).

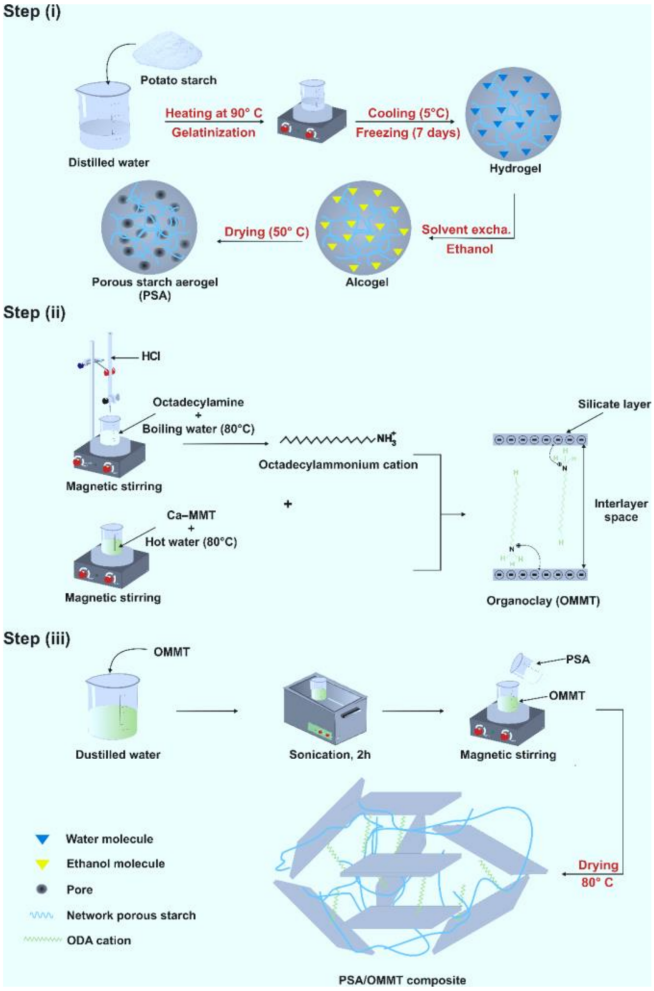

Figure 1. Schematic illustration of the synthesis route of PSA/OMMT composites.

2.3. Adsorbent Characterizations

Intercalation of organic materials, *d*-spacing, and crystalline structure of composites were all investigated using X-ray diffraction (XRD) measurements using a Bruker D8 Advance AXS diffractometer equipped with a *CuKα* radiation source (λ = 1.5418 Å). The instrument operates at 40 kV and 30 mA, and the data acquisition was conducted in the 2θ range of 1.5–40° at a scan step size of 0.019° and 109.8 s counting time per step. Bragg's

law, defined as $\lambda = 2d.sin\theta$, was used to compute the crystallographic spacing (d) of the samples. The changes in surface functional groups on PSA and Ca-MMT samples were investigated using a Fourier-transform infrared (FTIR) spectrometer (Thermo Electron Corporation, Nicolet 2000, Madison, WI, USA). Scans were recorded in transmittance mode in the wavelength range of 400–4000 cm^{-1} with a spectral resolution of 1 cm^{-1} in ambient air by the KBr pellet method and the instrument was coupled with OMNIC software for peak analysis. The effect of organoclay on the surface morphology of porous starch was performed using scanning electron microscopy (SEM). SEM micrographs were collected on TS Quanta 250 microscope operated at an accelerating voltage of 15 kV. Nitrogen adsorption–desorption of samples was carried out at 77 K using BET surface area and pore volume analyzer (Micromeritics, ASAP 2020, Norcross, GA, USA) to determine the textural properties such as specific surface area, total pore volume, and average pore diameter. The thermal behavior of the samples was determined by thermogravimetric analysis (TGA) on an SDT Q600 instrument, within the range of 30–600 °C at a heating/cooling rate of 10 °C/min under a N_2 atmosphere.

2.4. Batch Adsorption Study

Typical anionic dye methyl orange (MO) was used to evaluate the adsorption properties of the synthesized PSA/OMMT composite. In brief, 20 mg of PSA/OMMT powder was added to 20 mL of MO aqueous solution in batch mode. Then, the mixed solution was stirred at 420 rpm at room temperature and the samples were centrifuged at 4000 rpm for 15 min to separate the solids from the liquid phase before being examined using UV-vis spectrophotometry (T60 UV Visible Spectrophotometer, PGI, China). The concentrations of dye in the supernatant (C_e) were determined eventually from the calibration plot of C_0 vs. absorbance at 463 nm (Figure S1). The MO removal rate and the loading amount of dye adsorbed at equilibrium (Q_e) were calculated according to the following Equations (1) and (2), respectively:

$$Removal\ rate\ (\%) = \frac{C_0 - C_e}{C_0} \times 100 \quad (1)$$

$$Q_e = (C_0 - C_e)\frac{V}{m} \quad (2)$$

where C_0 and C_e (mg/L) are the initial concentration and the equilibrium concentration of dye, respectively, V (L) is the volume of the dye solution, and m (mg) is the weight of PSA/OMMT.

Above all, experimental parameters including pH solution (3–10), reaction time (5–90 min), and adsorbent dosage (20–100 mg) were carefully refined to achieve maximum adsorption. Under optimized conditions, the adsorption capacity of PSA/OMMT for MO was measured over a set of initial dye concentrations (50–400 mg/L). Moreover, the adsorption capacity was investigated using adsorption thermodynamics at 25, 30, 35, 40, and 45 °C in a thermostatic bath.

All experiments were performed in triplicate. Data were analyzed using a one-way analysis of variance followed by a mean test.

2.5. Reusability Test

To access the practical application of the PSA/OMMT adsorbent, the regeneration tests were carried out through adsorption–desorption cycles. Initially, adsorption of 350 mg/L of MO was made on 20 mg PSA/OMMT as described above, afterwards, the desorption cycle was allowed by immersing in 96% ethanol. The suspension of PSA/OMMT was stirred for 2 h and then separated by washing/centrifugation at a speed of 4000 rpm for 5 min. This process was repeated 3 times and the regenerated PSA/OMMT was dried overnight at 80 °C and rehydrated into the same volume of the dye solution (350 mg/L).

3. Results and Discussion

3.1. Characterizations of PSA/OMMT

3.1.1. X-ray Diffraction Analysis

The structural information was verified using the powder X-ray diffraction technique. Figure 2A shows the XRD pattern of the starch samples. Native starch (NS) exhibited a B-type crystalline pattern, with major peaks at 2θ of 10.1°, 11.5°, 14.0°, 15.1°, 17.2°, 19.7°, 22.1°, and 24.1°, and minor peaks at about 26.4°, 31.3°, and 34.7°, which is characteristic of native regular potato starch [31,32]. However, some changes could be observed in the XRD pattern of PSA. A slight decrease can be observed in the crystallinity mainly due to the starch gelatinization and degradation. PSA had sharp diffraction peaks at 2θ of 17.3°, 19.6°, 22.3°, 30.5°, and 34.1°, indicating that the gelatinization process attacks the crystalline region, which possibly prevented the recrystallization of degraded polysaccharide chains. Therefore, the gelatinization of NS could be accompanied by the retrograded phenomenon of starch. Numerous studies found similar findings upon treatment of corn/cassava/potato starches where diffraction peaks were less sharp or even disappeared compared to their native counterparts [33,34].

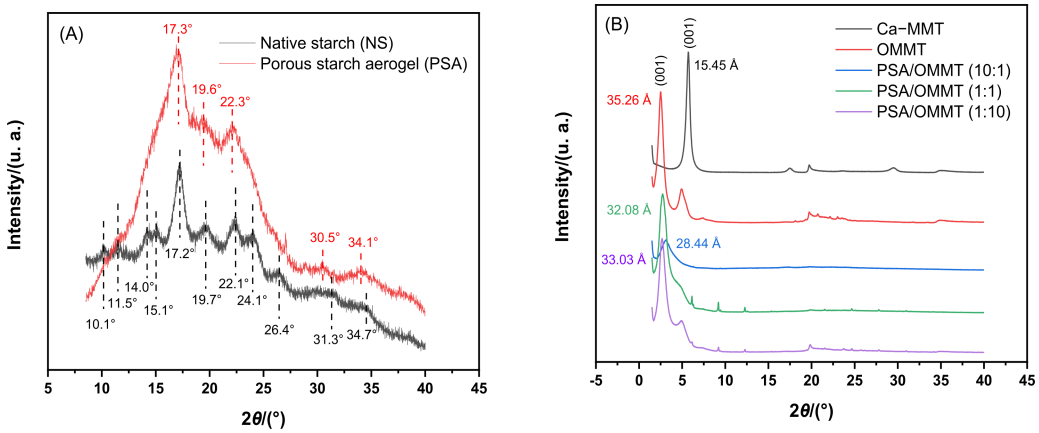

Figure 2. XRD diffractograms of (**A**) the starch samples and (**B**) the Ca-MMT pristine clay, organoclay, and starch–organoclay composites.

Furthermore, Figure 2B exhibits the XRD patterns of the clay, organoclay, and starch–organoclay interactions. The pristine clay displayed the typical XRD pattern of Ca-MMT with an intense diffraction peak at 2θ of 5.7°, corresponding to the clay interlayer spacing value d_{001} of 15.45 Å according to Bragg's law [35]. However, in the OMMT, a displacement of the peak to the lower angles (2.5°) is observed with an increase in the interlayer distance up to 35.26 Å, confirming thus the successful intercalation of the ODA surfactant within the clay layers. Likewise, the 001 diffraction peak in the composite samples was shifted to comparable lower angle values of 3.1° (28.44 Å), 2.7° (32.08 Å), and 2.6° (33.03 Å) for the different ratios of 10:1, 1:1, and 1:10, respectively. This difference in the interlayer spacing values is attributed to the partial exfoliation and dispersion of OMMT nano-platelets within the porous starch matrix due to the strong polar interaction between the hydroxyl groups of polysaccharide chains and OMMT. Furthermore, the composite patterns revealed the vanishing of the porous starch peaks, which indicates that the polymer chains could enter between the silicate platelets without reaching complete exfoliation. The literature has already revealed similar trends for starch/MMT interaction [22,23]. Further analysis based on the Sherrer Equation (3) can confirm our findings where the corresponding average number of ordered layers ($\overline{M}$) in the composites 10:1, 1:1, and 1:10 was found to be 3, 4, and 6, respectively, compared to a respective 18 and 10 layers in the clay and organoclay.

$$\overline{M} = \frac{\lambda \cdot K}{d_{001} \times \Delta 2\theta_{001} \times cos\theta_{001}} \quad (3)$$

where K is the Scherrer constant (0.91), λ is the X-ray wavelength (1.5418 Å), θ is the angle of the 001 peaks (°), and $\Delta 2\theta$ is the full width at half maximum of the 001 reflections (rad).

3.1.2. Fourier Transform Infrared Spectroscopy

The functional groups present in the PSA/OMMT composite and its precursor are shown in Figure 3. The PSA spectrum contains a broad peak at around 3408 cm^{-1} corresponding to the hydroxyl stretching vibration in the polysaccharide chain [36], 2 narrow peaks at 2925 and 1639 cm^{-1} attributed, respectively, to the C–H stretching of the CH_2 groups in the amylose/amylopectin-rich polymer and the adsorbed water [23], and 3 further peaks at 1156, 1028, and 928 cm^{-1} that can be associated with the C–O, and C–O–C stretching vibrations in the α-1,4 glycosidic linkage [36]. The characteristic absorption bands for Ca-MMT clay appear at about 3627, 3417, 1642, 1042, 532, and 460 cm^{-1}, whereas, for OMMT bands appear at 3627, 3417, 2919, 2848, 1642, 1516, 1467, 1042, 532, and 460 cm^{-1}. The common peaks at 3627 and 3417 cm^{-1} can be attributed to the –OH stretching vibrations attached to Al^{3+} in the octahedral layer and the interlayer water molecule, respectively [18,23], while the absorbance at 1642 cm^{-1} arises due to the adsorbed water molecule. The absorption bands appearing at 1042, 532, and 460 cm^{-1} can be assigned to the intrinsic vibrations of tetrahedral and octahedral sites Si–O, Al–O, and Si–O–Al inside the clay sheets [18,23]. However, the appearance of 3 additional peaks at 2919, 2848, and 1467 cm^{-1} in the case of OMMT indicates the presence of intercalated ODA surfactant. Bands at 2919 and 2848 cm^{-1} are attributed to the C–H asymmetric and symmetric stretching vibrations of octadecylamine, respectively, and the band at 1467 cm^{-1} is assigned to the ammonium salt [29]. Upon interaction of porous starch matrix with organoclay, characteristic peaks of starch (–OH, C–H, C–O, and C–O–C) were identified, as well as functional groups previously found in the organically modified clay spectrum corresponding to Al–OH, Si–O, Al–O, and Si–O–Al. Meanwhile, composite spectra depict a slight shift to close but different wavelengths in the Si–O and –OH bands, suggesting a strong hydrogen-bonding site in both the organoclay surface and gallery for starch molecules [18,37], which caused the exfoliation/delamination of clay. Otherwise, the broadening of the peaks and the increasing of their intensity can be explained by the different starch-to-organoclay ratios (SN). These results further confirmed those deduced from XRD investigation and compiled as well with the data reported in the literature [18].

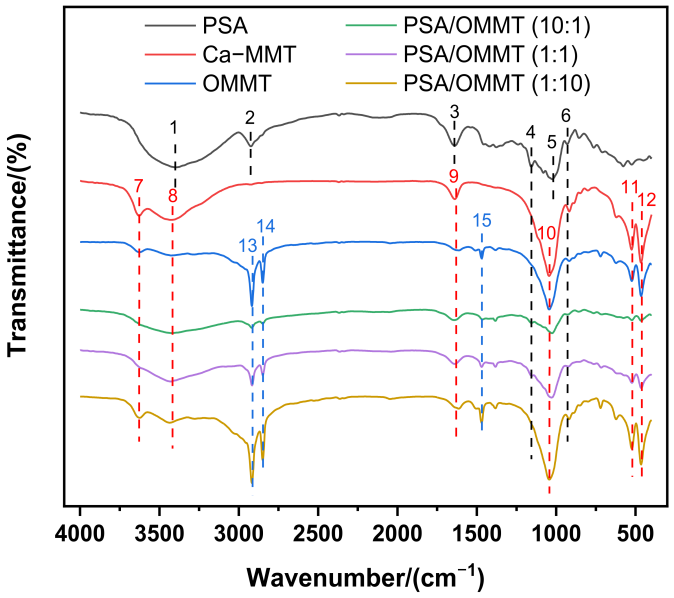

Figure 3. FTIR spectra of PSA, Ca-MMT, OMMT, and PSA/OMMT composites. The dashed lines mark the peaks: 3408 (1), 2925 (2), 1639 (3), 1156 (4), 1028 (5), 928 (6), 3627 (7), 3417 (8), 1642 (9), 1042 (10), 532 (11), 460 (12), 2919 (13), 2848 (14), and 1467 (15) cm^{-1}.

3.1.3. Scanning Electron Microscopy

Figure 4 shows SEM micrographs of the surface morphology of PSA (top) and the PSA/OMMT composite (1:10) (bottom). The surface of the porous starch exhibits many wrinkles due to the evolution of the NS upon the gelatinization process, which leads to the formation of pores on the surface. These are responsible for the porous structure of the starch which makes it more suitable for surface chemical modification than NS. However, after incorporating the organoclay into the porous starch matrix, a relatively heterogeneous dispersion of the nanolayers with no large aggregates is observed, attesting to an exfoliated morphology, which is in good agreement with the results obtained from XRD analyses. Thus, from this investigation, the PSA/OMMT composite can be assumed to have an enhanced specific surface area and stable adsorption capacity.

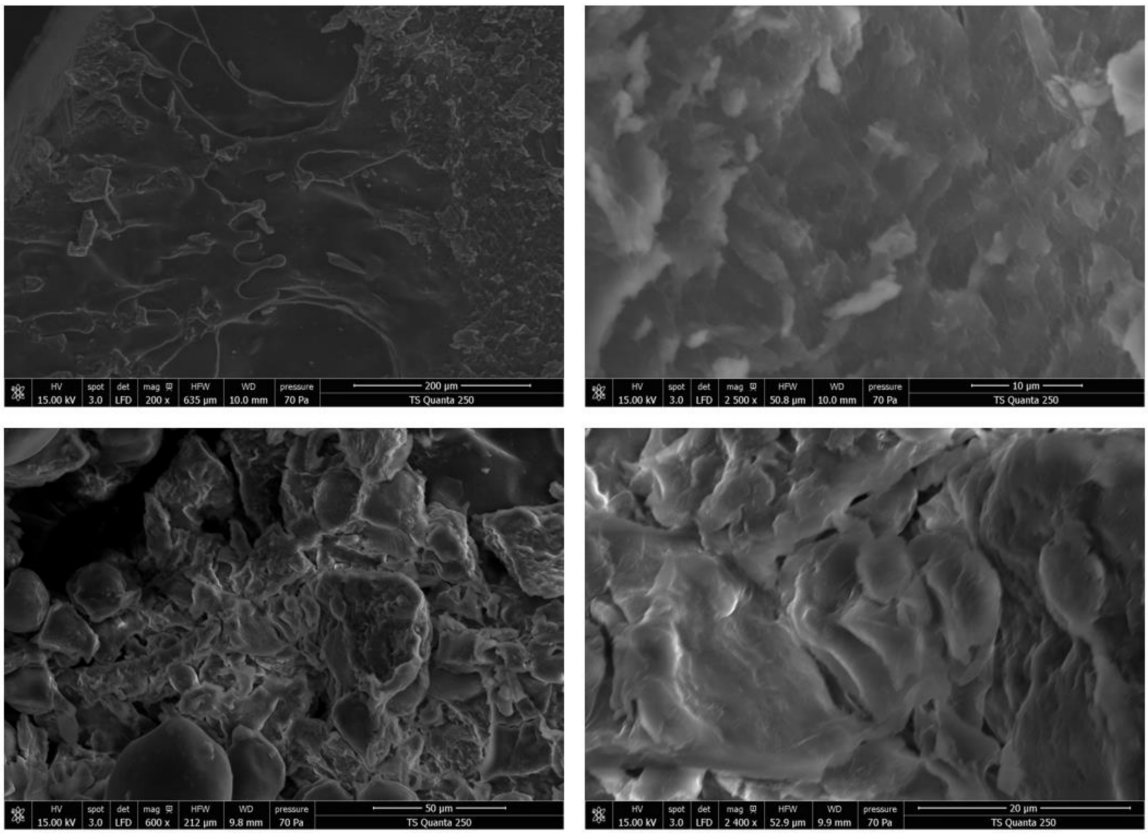

Figure 4. SEM images of PSA (**top**) and PSA/OMMT (**bottom**) composite (1:10).

3.1.4. Nitrogen Adsorption–Desorption

To gain insight into the textural properties of the PSA/OMMT composite, the N_2 adsorption–desorption analyses of the porous starch and composite (1:10) were recorded at 77 K. Figure 5 shows the N_2 adsorption–desorption isotherms within the relative pressure P/P_0 range of 0.05–1.0. Both materials exhibit a typical II isotherm feature with H3 hysteresis loops at a relatively high-pressure range, according to the IUPAC classification [38]. The Brunauer-Emmett-Teller (BET) specific surface area of the porous starch was calculated to be about 6.10 m^2/g, while that of the composite (1:10) was estimated to be about 18.77 m^2/g. This increased surface area can be attributed to a higher dispersity of organoclay into the porous starch matrix due to a strong hydrogen bonding between the two components. On the other hand, the total pore volume and average pore size were approximately 2.06 cm^3/g and 11.30 nm for PSA and 0.59 cm^3/g and 15.16 nm for composite (SN 1:10), respectively, as predicted by the Barrett-Joyner-Halenda (BJH) analytical model (Table 1). This decrease in the pore volume of modified porous starch was observed due to the pore blocking by modifiers upon modification. This pore blocking was entirely dependent on the high

dispersion of the organoclay sheets within the matrix. Thus, it is obvious that the starch-organoclay interaction significantly influenced the surface area and porosity, which makes the composite a promising adsorbent for MO dyes.

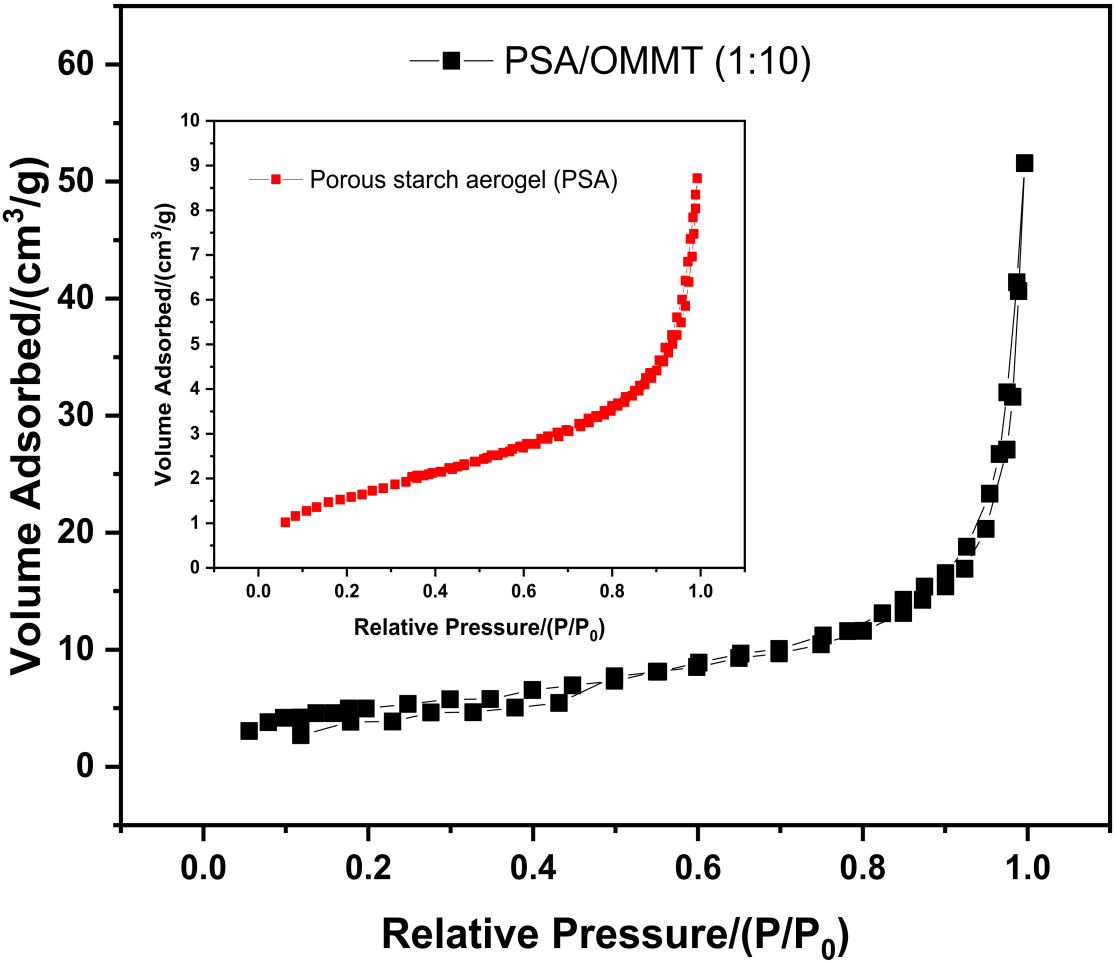

Figure 5. N_2 adsorption–desorption isotherms of PSA and PSA/OMMT composite (1:10).

Table 1. Surface area and pore size PSA and PSA/OMMT composite (1:10).

Samples	BET Surface Area (m^2/g)	Pore Volume (cm^3/g)	Pore Size (nm)
PSA	6.10	2.06	11.30
PSA/OMMT (1:10)	18.77	0.59	15.16

3.1.5. Thermogravimetric Analysis

Thermogravimetric analysis was performed to provide information on the thermal stability of the PSA matrix before and after interaction with the organoclay layers, and results are shown in Figure 6. Table 2 shows the thermal stability parameters extracted from TGA thermograms. As can be seen, the initial decomposition temperature (T_d *i*) of PSA was 251.5 °C, and the addition of 10-fold OMMT pushed it above the T_d *i* to 274.2 °C, indicating thus an improvement in the stability of PSA. In addition, the thermal decomposition of PSA and PSA/OMMT is expressed in terms of weight loss. At temperatures below 100 °C, the water in the samples is the main cause of weight loss. When the decomposition temperature was reached, the weight decreased rapidly with the rise in temperature and then tended to stabilize. From 100 °C to T_d *i*, the weight loss rate was lower in the composite than in the porous starch due to the strong hydrogen binding between the exfoliated/delaminated

structure of organoclay and starch, which prevents the increased sensitivity of the thermal transition for starch, while the mass loss percentages were relatively close between $T_d\ i$ and $T_d\ f$ (the final decomposition temperature) owing to the organophilic character of the clay. However, the increase in the following weight loss stage of the composite ($T_d\ f$—600 °C) compared with starch is due to the decomposition of both starch and surfactant sub-products formed during the degradation. Nevertheless, these outcomes suggest that the thermal stability of the porous starch was basically enhanced.

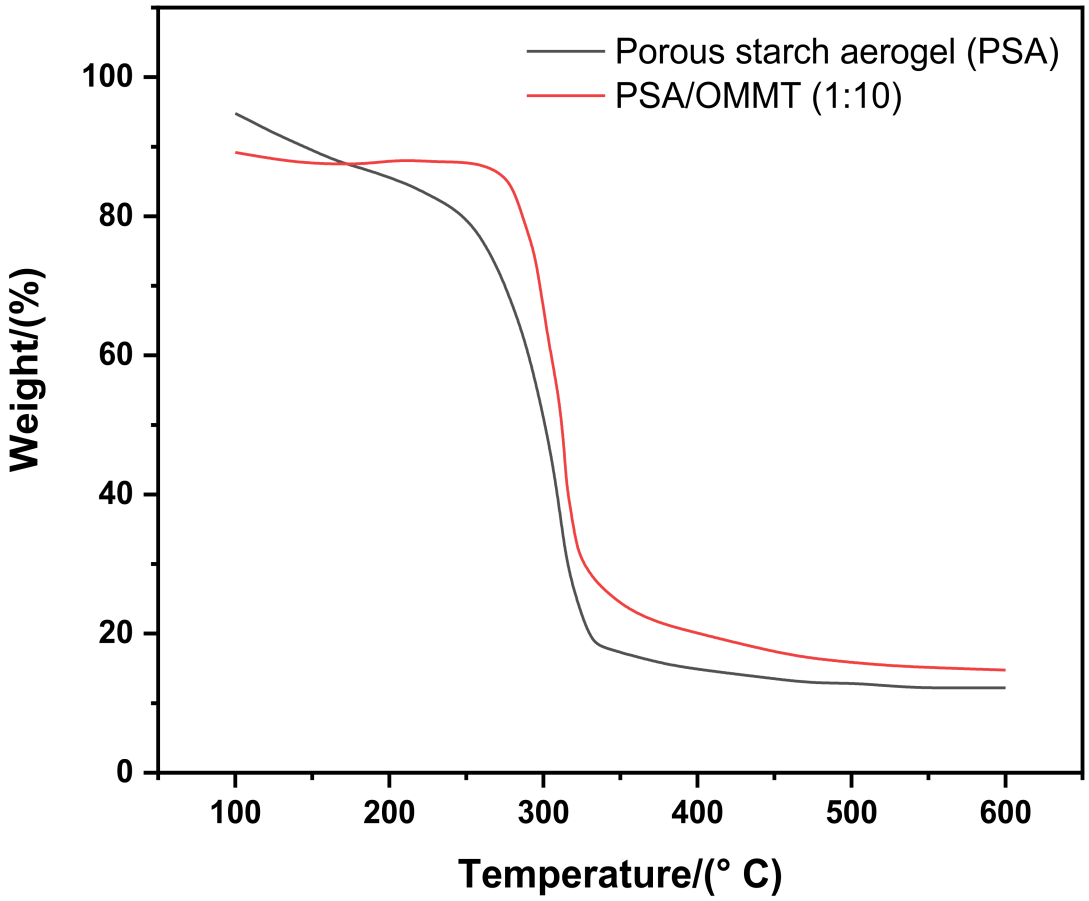

Figure 6. TGA curves of PSA and PSA/OMMT composite (1:10).

Table 2. Thermal stability parameters of PSA and PSA/OMMT composite (1:10).

Samples	T_d i (°C)	T_d f (°C)	Weight Loss (%)		
			100°—T_d i (°C)	T_d i—T_d f (°C)	T_d f—600 (°C)
PSA	251.5	332.9	13.8	62.5	6.04
PSA/OMMT (1:10)	274.2	337.6	2.8	58.6	12.9

3.2. Batch Adsorption Study

3.2.1. Optimization of Experimental Parameters

Numerous research studies indicated that clay incorporation might enhance the adsorption ability of starch materials toward dye pollutants [18,39]. A similar observation was also made in this study (Figure 7A), where porous starch showed the lower adsorption performance towards MO dyes, with a removal efficiency of 38.4%, while all composite adsorbents (10:1), (1:1), and (1:10) outperformed the starch matrix in terms of removal rate under similar conditions, with percentages of 42.5%, 96.7%, and 98.6%, respectively. However, the maximum removal percentage of MO was reached when the organoclay

content was 10-fold that of the starch. This can be attributed to the good correlation between the dispersion and the delamination/exfoliation behavior of organoclay in the PSA matrix while increasing the organoclay amount, which allowed for more active sites for adsorption compared with pure starch. Therefore, the composite with the starch-to-organoclay ratio (1:10) was chosen as the ideal adsorbent and used for further experiments.

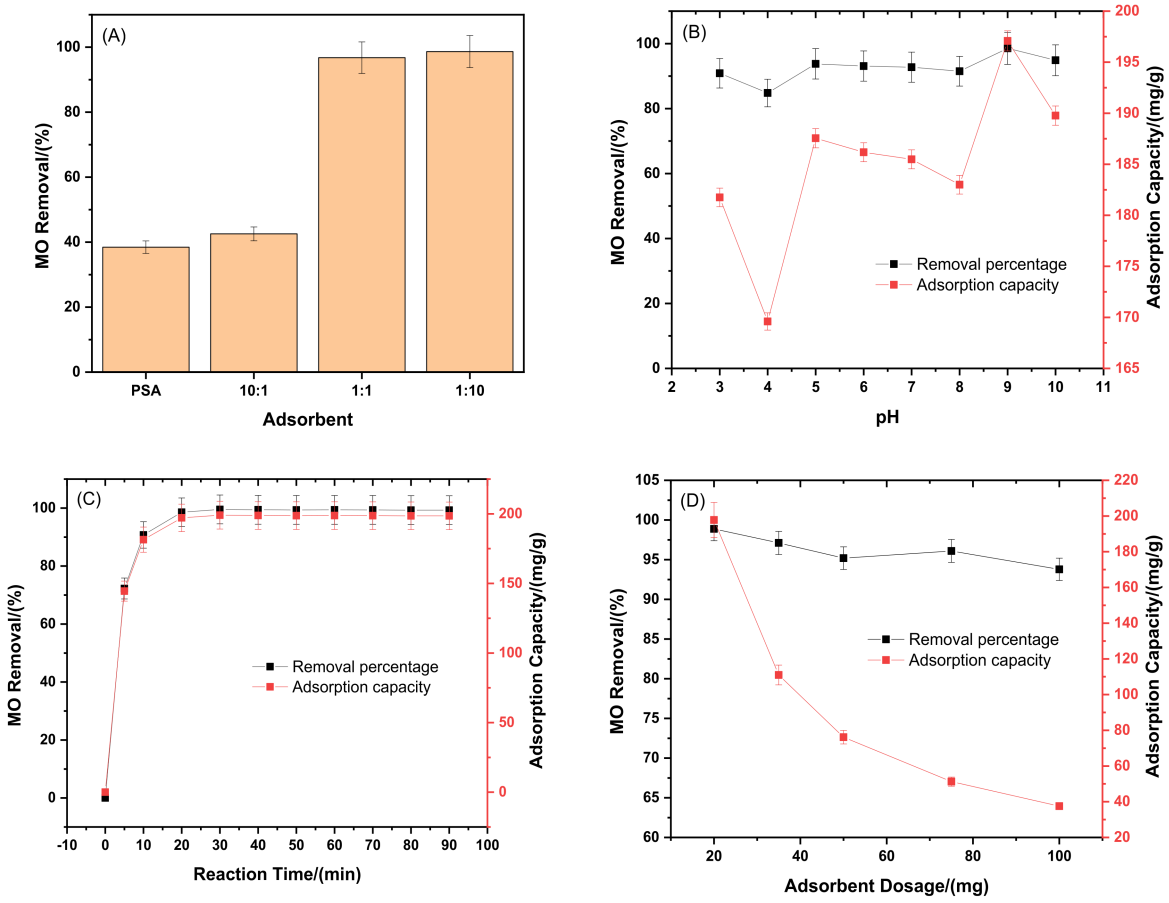

Figure 7. (**A**) Removal percentages of PSA and PSA/OMMT composites (10:1, 1:1, and 1:10) in 100 mg/L MO solution; (**B**) effect of pH solution, (**C**) effect of reaction time, and (**D**) effect of adsorbent dosage on the removal percentage and adsorption capacity of the composite (1:10) in 200 mg/L MO solution.

In order to achieve the best adsorption ability, various experimental parameters such as solution pH, reaction time, and adsorbent dosage were also investigated. Figure 7B displays the investigation results for the effect of pH in the range of 3–10, as the ionization of adsorbate and adsorbent surface charge are influenced by pH [40]. As depicted in Figure 7B, the removal percentage and adsorption capacity were relatively weak at pH 3–4 (90.8–84.7% and 181.7–169.5 mg/g), increased moderately to remain almost constant at around (93.7–91.4% and 187.5–182.9 mg/g) between pH 5–8, and then increased once again to reach their peak at pH 9 (98.5% and 189.7 mg/g) before dropping to 94.8% and 189.7 mg/g, respectively, at pH 10. Given the quite low variation of the removal percentage and adsorption capacity values in the pH range from 3 to 10, it seems likely that the electrostatic interaction between adsorbent and MO dye plays a more significant role than solution pH. Hence, pH 9 was set as the optimal pH in the subsequent experiments. Another important parameter that strongly influences the adsorption reaction is the reaction time. Figure 7C shows the effect of the contact time on the removal percentage and adsorption capacity of the composite at regular time intervals of up to 90 min. A rapid adsorption phase within 20 min followed by a slower uptake phase was observed. This trend suggests the

occurrence of abundant adsorption sites on the composite that are available for interaction with the dye molecules at an initial stage. Following the progression of the adsorption process, the number of active sites available for binding decreased, leading to a slower increase in the adsorption rate and the establishment of a plateau due to an oversaturation on the adsorbent surface. This corresponded to an almost complete removal rate of 99.2% and an adsorption capacity of 198.5 mg/g, respectively. However, to ensure that the dynamic equilibrium is fully reached, the MO adsorption must be performed with a reaction time of 30 min, which can be considered a practical duration for the adsorption systems. Finally, and perhaps most importantly, proper selection of the adsorbent dosage is crucial because the available surface area and binding sites can affect the adsorption performance. Figure 7D shows the effect of adsorbent dosage on MO adsorption. The results showed that further increases in adsorbent dosage from 20 to 100 mg have a minimal effect on the removal efficiency (98.8–93.7%). In contrast, the adsorption capacity decreased drastically from 197.7 mg/g (at 20 mg) to 37.5 mg/g (at 100 mg). This trend is predictable due to the formation of excessive active sites on PSA/OMMT at higher adsorbent dosage, which leads to many vacant sites, while the number of adsorbate molecules remains constant. Considering the economic standpoint and the adsorption performance, 20 mg of adsorbent would be practical for application as the optimal dosage.

3.2.2. Adsorption Isotherms: Effect of Initial Dye Concentration

Figure 8A represents the variation of removal efficiency and adsorption capacity over the initial dye concentration (50–400 mg/L) at a temperature of 25 °C, contact time of 30 min, and with an adsorbent dosage of 20 mg. At a concentration below 320 mg/L, the PSA/OMMT adsorbent can adsorb almost all amounts of dye with a removal rate of more than 99%. However, with the increase in dye concentration beyond 320 mg/L, the removal efficiency began to drop up to 86.2% at the concentration of 400 mg/L with an adsorption capacity of 344.8 mg/g, resulting in the saturation of the adsorption sites due to the fixed amount of adsorbent dosage and the lack of vacant binding sites. This thus explains the drastic increment in adsorption capacity at lower equilibrium concentrations C_e, followed by a slower rate at higher C_e, defined by a plateau (Figure 8B).

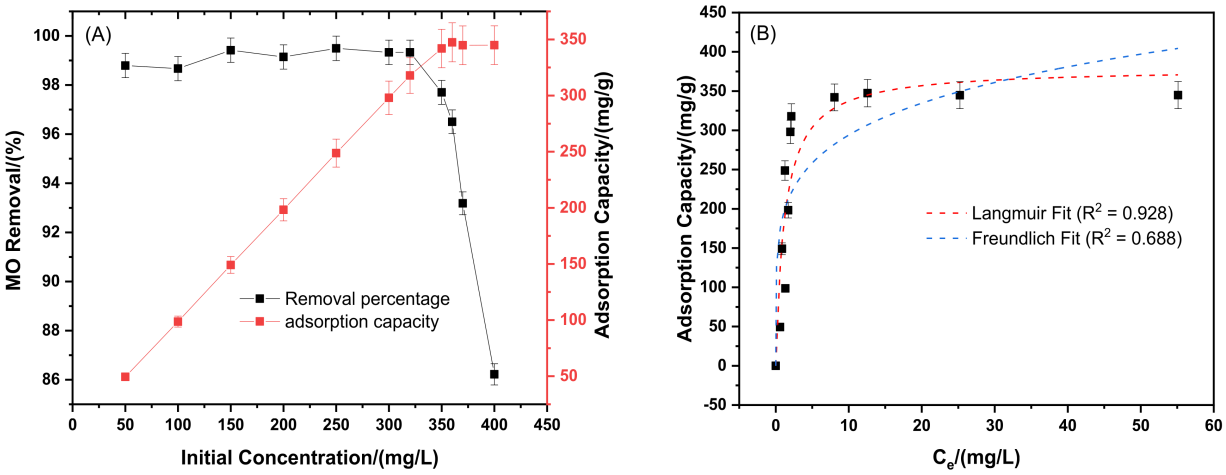

Figure 8. (**A**) Initial dye concentration effect on the removal percentage and adsorption capacity of PSA/OMMT composite (1:10) and (**B**) Langmuir and Freundlich isotherm plots for adsorption of MO dyes.

In order to predict the adsorption capacity of PSA/OMMT adsorbent and to further understand how the interaction between the adsorbent and adsorbate occurs, the equilibrium adsorption data were fitted with Langmuir and Freundlich isotherm models (Figure 8B).

The Langmuir model (4) assumes monolayer adsorption of solute on the homogenous surface of the adsorbent, containing a finite number of adsorption sites, and each site is

likely able to bind one solute molecule [41]. Whereas, the Freundlich model (5) is based on the multilayer adsorption of solute on heterogeneous binding sites [42].

$$Q_e = \frac{Q_m K_L C_e}{1 + K_L C_e} \tag{4}$$

$$Q_e = K_F C_e^n \tag{5}$$

where Q_m (mg/g) is the maximum monolayer adsorption capacity, K_L (L/mg) refers to the Langmuir equilibrium constant related to the adsorption rate, and K_F (L/g) and n are the Freundlich constants for adsorption capacity and strength, respectively.

The detailed fitting parameters of the Langmuir and Freundlich models are given in Table 3. As shown in Figure 8B and based on Table 3, the plot for the Langmuir isotherm fitted the experimental data better than that of Freundlich as indicated by the higher R^2 value (0.928) and the predicted adsorption capacity quite close to the experimental result (344.7 mg/g), implying thus that a uniform monolayer adsorption behavior is preferable for MO dye molecules. Meanwhile, the adsorption capacity of PSA/OMMT was matched with other previously reported adsorbents, and the results are enumerated in Table 4. It can be clearly observed that the adsorption capacity of the PSA/OMMT used in this study was rather higher compared with those of other studies, with an adsorption capacity of 344.7 mg/g. Hence, PSA/OMMT can be used as an efficient adsorbent for treating methyl-orange-containing wastewater.

Table 3. Langmuir and Freundlich parameters.

Fitting Parameters	Langmuir	Freundlich
Q_m (mg/g)	379.026	
K_F (L/g)		191.284
R^2	0.928	0.688

Table 4. Comparison of adsorption capacity of different adsorbents for MO.

Adsorbent	Q_m (mg/g)	Reference
Lapindo volcanic mud	333.33	[43]
Mesoporous carbon CMK-3	294.1	[44]
Polyaniline	75.9	[45]
CS/REC/CNT	41.65	[46]
Zn/Al LDH	276.55	[47]
Date palm ash/MgAl-LDH	242.98	[48]
AM-PIM-FM	312.5	[49]
CTA-CSM	131.9	[50]
Biochar from grape seeds	111.11	[51]
MnO_2/biomass from *Terminalia ivorensis*	81.32	[52]
PSA/OMMT (1:10)	344.7	this study

CS: chitosan; REC: rectorite; CNT: carbon nanotube; LDH: layered double hydroxide; AM-PIM-FM: amine-modified polymers of the intrinsic microporous fibrous membrane; CTA-CSM: quaternary ammonium salt-modified chitosan microsphere.

3.2.3. Adsorption Kinetics

In order to elucidate the mechanism that takes place during the adsorption of MO by the PSA/OMMT composite, the time-resolved adsorption capacity dataset was fitted in the pseudo-first-order (6), pseudo-second-order (7), and intra-particle diffusion model

kinetics (8). The pseudo-first-order assumes a physisorption-controlled process in which the rate of adsorption increases in direct proportion to the total number of vacant sites [53], while the pseudo-second-order is based on a chemisorption process and presumes that the rate of adsorption of adsorbate at the binding site is directly proportional to the square number of unoccupied sites [54]. Due to the porous nature of the PSA/OMMT composite, the time-resolved adsorption capacity data were also correlated with the intra-particle diffusion model, which considers the pore diffusion of adsorbate as the rate-limiting step [55]. The linearized equations of the three models are expressed below:

$$ln\ (Q_e - Q_t) = ln\ Q_e - \frac{k_1}{2.303}t \quad (6)$$

$$\frac{t}{Q_t} = \frac{1}{k_2 Q_e^2} + \frac{t}{Q_e} \quad (7)$$

$$Q_t = a - k_{int}t^{0.5} \quad (8)$$

where Q_t (mg/g) is the time-resolved adsorption capacity, t (min) is the reaction time, k_1 (min^{-1}), k_2 (g/mg·min), and k_{int} (mg/g·$min^{0.5}$) refer to the pseudo-first-order, pseudo-second-order, and intra-particle diffusion rate constants, respectively, and a represents the constant related to boundary layer thickness.

Figure 9 showed the linear fitting results of the three kinetic models, and the fitting parameters are included in Table 5. As can be seen from Figure 9 and Table 5, the adsorption process of MO by PSA/OMMT composite is best fitted to the pseudo-second-order model (Figure 9B) with an R^2 value of 0.999, suggesting a chemisorption process rather than physisorption in this case. Moreover, the calculated Q_e (201.6 mg/g) by the pseudo-second-order kinetic model agreed well with the experimental Q_e (198.6 mg/g), which further confirmed the suitability of the pseudo-second-order kinetic model. In contrast, the intra-particle diffusion model proceeds in two stages: the first stage corresponds to the external and intra-particle diffusion with a high adsorption rate (as denoted by the large intercept of the straight line), due to the occurrence of a high number of binding sites, while the second stage is almost horizontal due the lack of active sites, which related to the equilibrium. These results indicate that the adsorption process may involve some intra-particle diffusion. Hence, we can consider that the adsorption process of MO on PSA/OMMT composite is primarily governed by chemical adsorption and assisted by intra-particle diffusion.

Table 5. Adsorption kinetic parameters for MO.

Kinetic Model	Parameter	Value
Pseudo-first-order	k_1 (min^{-1})	0.51
	Q_e (mg/g)	58.8
	R^2	0.747
Pseudo-second-order	k_2 (g/mg·min)	0.0053
	Q_e (mg/g)	201.6
	R^2	0.999
Experimental Q_e (mg/g)		198.6

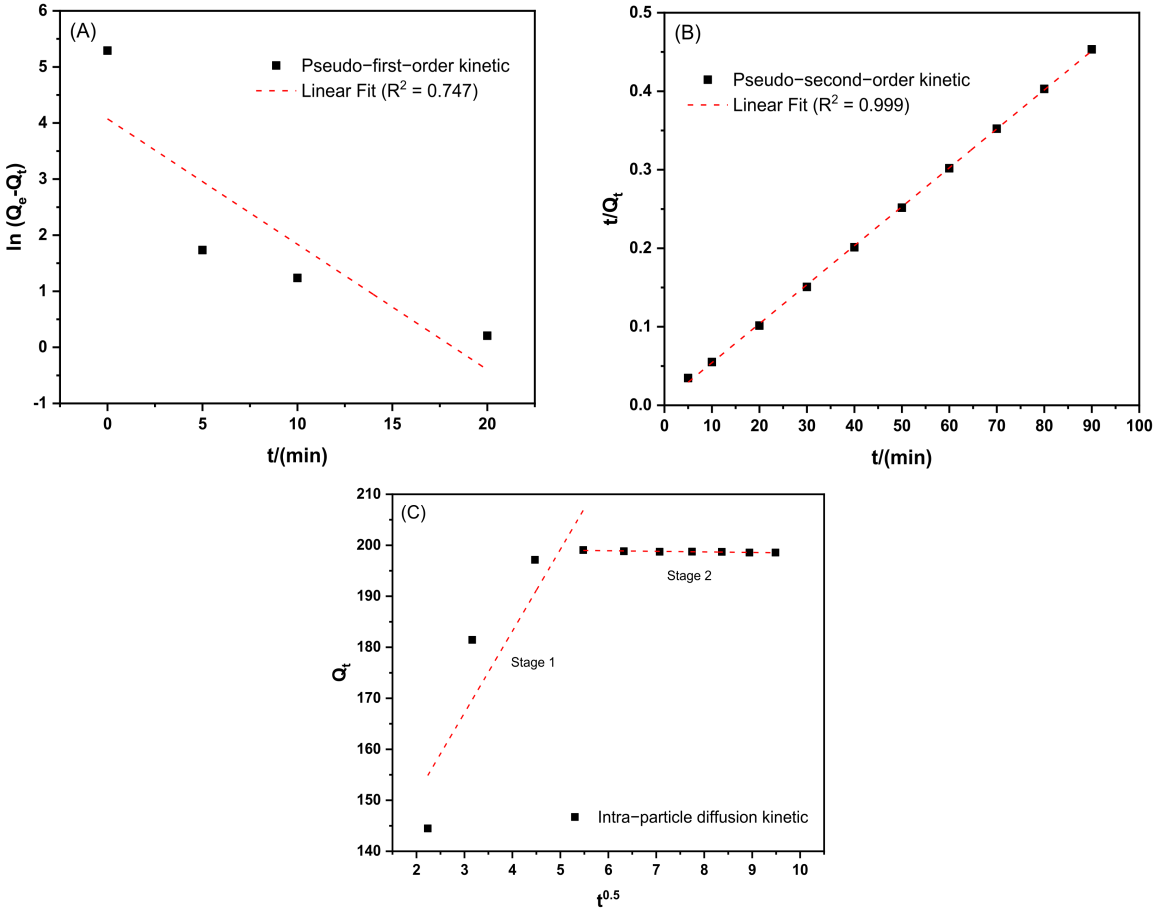

Figure 9. Adsorption kinetics: (**A**) pseudo-first-order, (**B**) pseudo-second-order, and (**C**) intra-particle diffusion for MO.

3.2.4. Adsorption Thermodynamics

Temperature is an essential parameter to identify the nature of the adsorption process and discover whether it is endothermic or exothermic. In this context, thermodynamic experiments were carried out at 25, 30, 35, 40, and 45 °C with an initial dye concentration of 350 mg/L. The effect of temperature on removal efficiency and adsorption capacity of PSA/OMMT for MO is illustrated in Figure 10A. It was demonstrated that the removal rate and adsorption capacity decreased from 97.7% and 341.9 mg/g to 83.9% and 293.2 mg/g with increasing temperature from 25 to 45 °C, respectively, indicating the exothermic nature of MO uptake. This result proves that heat caused lower surface energy on the adsorbent surface, which leads to lower collision and binding forces between the adsorbate and adsorbent. By calculating the thermodynamic parameters of the adsorption process such as Gibbs free energy change ΔG° (kJ/mol), enthalpy change ΔH° (kJ/mol), and entropy change ΔS° (J/mol·K), the thermodynamic behavior of MO adsorption process is deeply elucidated. The relevant thermodynamic parameters were evaluated using the Van 't Hoff plot (Figure 10B) and reported in Table 6.

$$ln\ K_0 = \frac{\Delta S^\circ}{R} - \frac{\Delta H^\circ}{RT} \quad (9)$$

$$\Delta G^\circ = RT\ ln\ K_0 \quad (10)$$

$$K_0 = \frac{Q_e}{C_e} \quad (11)$$

where T (K) is the temperature, and R (8.314 J/mol·K) is the molar gas constant.

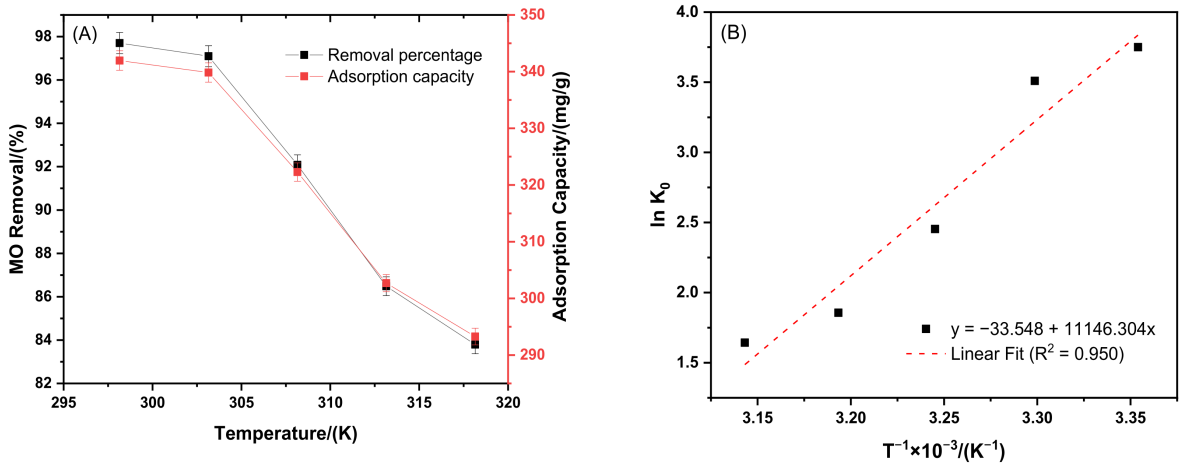

Figure 10. (**A**) Temperature effect on the removal percentage and adsorption capacity and (**B**) Van 't Hoff plot of MO dye onto PSA/OMMT composite (1:10).

Table 6. Thermodynamic parameters for MO adsorption onto PSA/OMMT.

Parameter		Value
ΔG° (kJ/mol)	298 K	−9.30
	303 K	−8.84
	308 K	−6.27
	313 K	−4.81
	318 K	−4.33
ΔH° (kJ/mol)		−92.67
ΔS° (J/mol/K)		−278.91

Negative values of ΔG° at all temperatures indicate that the adsorption process of MO on the PSA/OMMT composite is spontaneous. In addition, the ΔG° values are within the range of −20 to 0 kJ/mol, which suggests plausible physical adsorption for MO. The negative value of ΔH° confirmed further the exothermic nature of the adsorption reaction and the $\Delta S^\circ < 0$ indicated that this adsorption process is an entropy-decreasing process, which reflects the decreasing randomness at the solid–solution interface.

3.3. Adsorption Mechanism

The adsorption process usually depends on the physicochemical properties of the adsorbent surface (chemical surface and functionalities) and adsorption data (pH, kinetic, isotherm, and thermodynamic studies). The adsorption process of MO by the PSA/OMMT composite had been confirmed to be particularly a monolayer chemical adsorption. However, the initial pH of the solution slightly reinforced the MO uptake, which points to the electrostatic mechanism as the major contributor to the MO removal. Looking closely (Figure 11), the surface of the PSA/OMMT composite contains a large number of protonated ($-NH_2$) groups coming from octadecyl ammonium cations, that is, positively charged groups electrostatically attracting the negatively charged sulfonic acid group ($-SO_3^-$) on MO dye species. At the same time, the hydroxyl groups on the PSA/OMMT surface can coordinate with the N-containing groups on methyl orange, leading thus to dipole–dipole H-bonding interactions. This may also overlap with methyl orange and form Yoshida H-bonding, which reinforced the adsorption process. Furthermore, the possibility of n-π stacking interaction cannot be denied. The n-π stacking interaction usually occurrs when

the lone pair of electrons on an oxygen atom is delocalized into the π orbital of the aromatic ring of dyes [50,56]. Hence, n-π stacking interactions are likely to play a role in dictating MO adsorption.

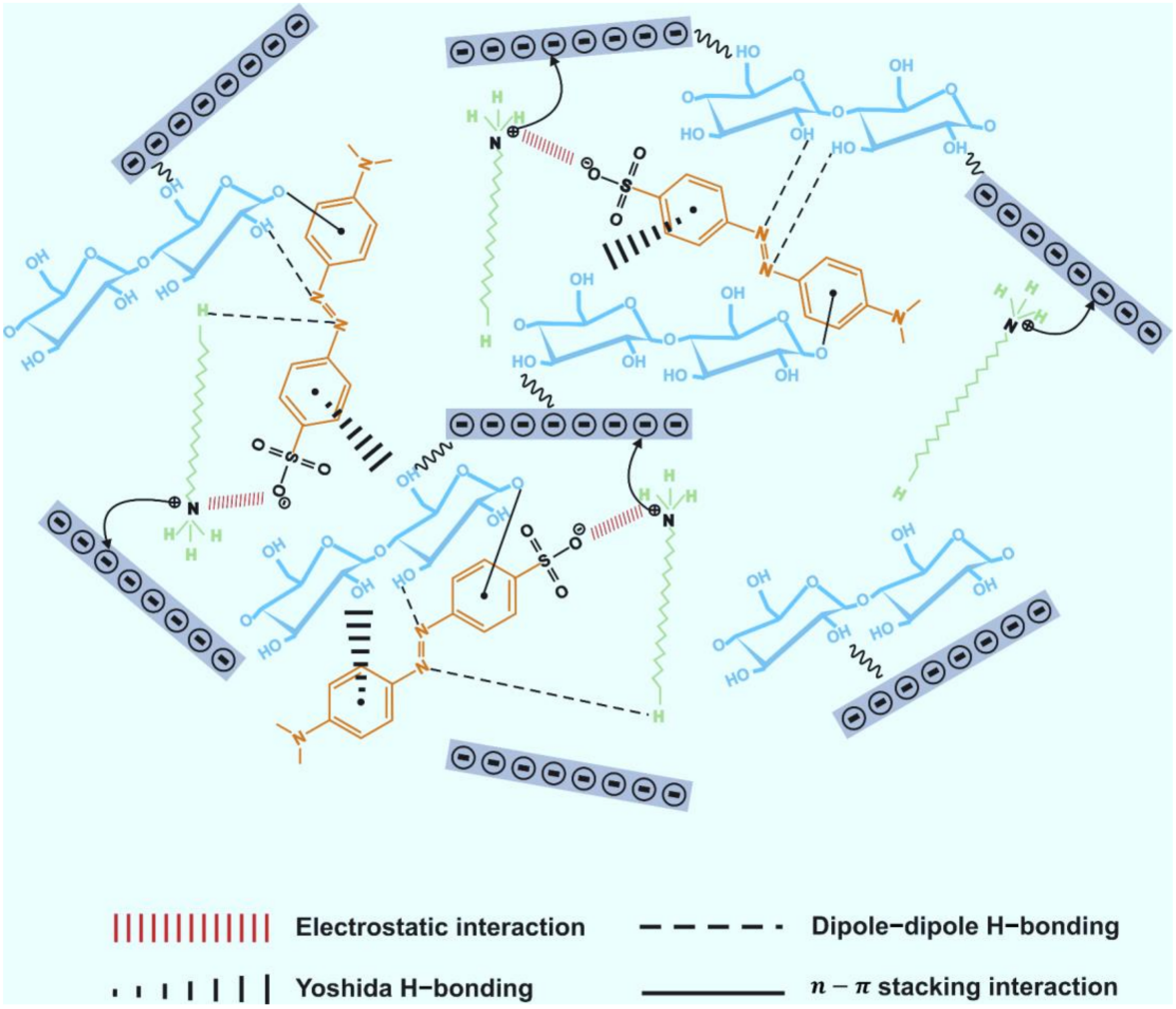

Figure 11. Illustration of MO adsorption onto PSA/OMMT composite.

3.4. Reusability Study

The recyclability and reusability of the adsorbent are important factors in sustainable and practical applications. Thus, the regeneration and reusability of PSA/OMMT adsorbent were performed using consecutive adsorption–desorption experiments and the result is shown in Figure 12. It can be seen that although the removal percentage gradually decreased with an increase in cycle time, the removal rate still reached 84.7% after 5 cycles. The slight drop in removal rate is perhaps because some MO molecules were tightly adsorbed on the adsorbent and could not be desorbed completely. Overall, the PSA/OMMT composite showed good adsorption performance and good cycling stability, which make it attractive and reliable in the practice of treatment of dyeing wastewater.

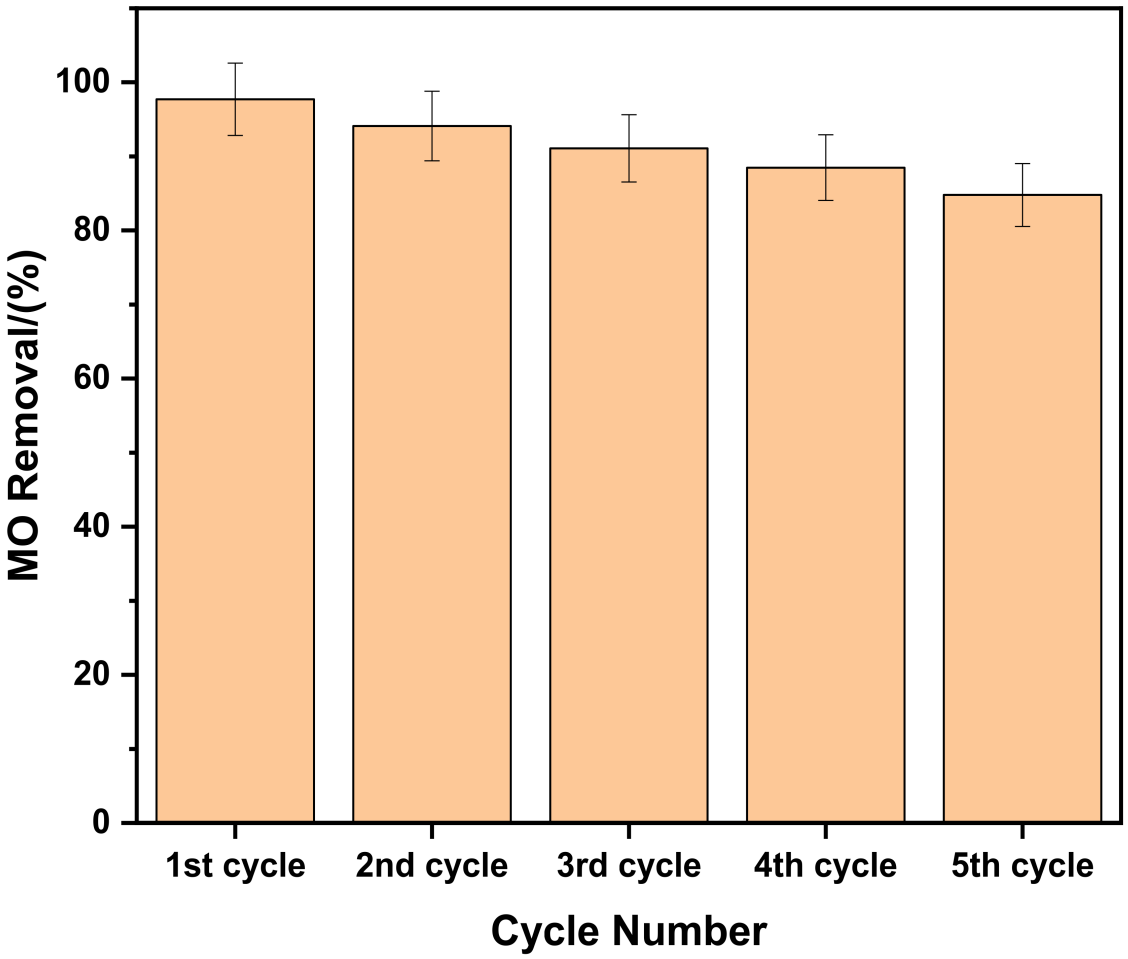

Figure 12. Recycle usability of PSA/OMMT adsorbent.

4. Conclusions and Future Outlook

Overall, the PSA/OMMT composite based on the natural porous starch and the organically modified montmorillonite is yielding innovative and effective adsorbent for methyl orange dyes. The adsorption performance of PSA/OMMT on MO-simulated dyeing wastewater was investigated in detail. The synergetic effect between the porous matrix and the organoclay layers was found to greatly improve the adsorption efficiency by 2.56 times over the virgin starch. The adsorption process followed the Langmuir isotherm model and the pseudo-second-order kinetic in which chemical adsorption was the main step, with an adsorption capacity of up to 344.7 mg/g, which was rather superior to those reported in the literature. Mechanism analysis showed that the MO uptake takes place largely through electrostatic attraction along with hydrogen bonding and *n*-π stacking interactions, which suggests that the interaction between the dye molecules and adsorbent involves physisorption before partitioning into the porous monolayer surface of the PSA/OMMT. In addition, the removal rate retained a value of 84.7% after 5 cycles of reusability, showing excellent recyclability performance, which qualified the PSA/OMMT to be an easily recoverable, cost-effective, and efficient adsorbent for dyeing wastewater treatment. However, when assessing prospects for potential upscaling of the synthesized PSA/OMMT, more adsorption investigation needs to be explored in multicomponent systems, in contrast to the current report. Since the material bears a variety of functional groups and charges, and dye wastewater often contains a variety of salts and organic pollutants, this can affect the adsorption performance. More mechanistic insights into water pollutant removal need to be understood in multicomponent simulated and real effluent systems to study the antagonistic effects restricting the development of an adsorbent

with high selectivity for the specific pollutants in order to improve real-world water quality challenges.

Supplementary Materials: The following supporting information can be downloaded at https://www.mdpi.com/article/10.3390/colorants2020014/s1, Figure S1: Calibration plot (A) and UV-vis spectrum (B) of MO.

Author Contributions: R.J.: Methodology and preparation, formal analysis, and visualization. M.A.D.: Investigation, data curation, supervision, writing, editing, and review. S.B.: Investigation. H.B.R.: Supervision, funding acquisition, and review. A.B.H.A.: Supervision, funding acquisition, and review. All authors have read and agreed to the published version of the manuscript.

Funding: This research received no external funding.

Acknowledgments: The authors would like to acknowledge all those who contributed their time and resources to the development of this work.

Conflicts of Interest: The authors declare no conflict of interest.

Abbreviations

MO	Methyl orange
MMT	Montmorillonite
Ca-MMT	Ca-activated montmorillonite
OMMT	Organically modified Ca-montmorillonite
NS	Native starch
PSA	Porous starch aerogel
ODA	Octadecylamine
XRD	X-ray diffraction
FTIR	Fourier-transform infrared
SEM	Scanning electron microscopy
BET	Brunauer–Emmett–Teller
BJH	Barrett–Joyner–Halenda
TGA	Thermogravimetric analysis
V(L)	The volume of the dye solution
m(mg)	The weight of PSA/OMMT
C_0 (mg/L)	The initial concentration of dye
C_e (mg/L)	The equilibrium concentration of dye
Q_e (mg/g)	The adsorbed quantity at equilibrium
Q_m (mg/g)	The maximum monolayer adsorption capacity
Q_t (mg/g)	The time-resolved adsorption capacity
K_F (L/g)	The Freundlich adsorption constant
K_L (L/mg)	The Langmuir adsorption constant
n	The Freundlich strength constant
k_1 (min^{-1})	The pseudo-first-order rate constant
k_2 (g/mg·min)	The pseudo-second-order rate constant
k_{int} ($mg/g \cdot min^{0.5}$)	The intra-particle diffusion rate constant
a	The constant related to boundary layer thickness
T (K)	Temperature
t (min)	The reaction time
T_d f (K)	The final decomposition temperature
T_d i (K)	The initial decomposition temperature
ΔG° (kJ/mol)	Gibbs free energy
ΔH° (kJ/mol)	Enthalpy
ΔS° (J/mol·K)	Entropy
R (8.314 J/mol·K)	The universal gas constant

References

1. Schwarzenbach, R.P.; Escher, B.I.; Fenner, K.; Hofstetter, T.B.; Johnson, C.A.; von Gunten, U.; Wehrli, B. The Challenge of Micropollutants in Aquatic Systems. *Science* **2006**, *313*, 1072–1077. [CrossRef] [PubMed]
2. Chatterjee, S.; Guha, N.; Krishnan, S.; Singh, A.K.; Mathur, P.; Rai, D.K. Selective and Recyclable Congo Red Dye Adsorption by Spherical Fe_3O_4 Nanoparticles Functionalized with 1,2,4,5-Benzenetetracarboxylic Acid. *Sci. Rep.* **2020**, *10*, 111. [CrossRef]
3. Jiang, R.; Yu, G.; Ndagijimana, P.; Wang, Y.; You, F.; Xing, Z.; Wang, Y. Effective Adsorption of Direct Red 23 by Sludge Biochar-Based Adsorbent: Adsorption Kinetics, Thermodynamics and Mechanisms Study. *Water Sci. Technol.* **2021**, *83*, 2424–2436. [CrossRef]
4. Zhang, T.; Yu, H.; Wang, W.; Bai, P.; Jin, K.; Zhang, J.-N.; Yan, W. Removal of Anionic Dyes from Aqueous Solution with Layered Cationic Aluminum Oxyhydroxide. *Chem. Res. Chin. Univ.* **2022**, *38*, 1532–1541. [CrossRef]
5. Wong, S.; Ghafar, N.A.; Ngadi, N.; Razmi, F.A.; Inuwa, I.M.; Mat, R.; Amin, N.A.S. Effective Removal of Anionic Textile Dyes Using Adsorbent Synthesized from Coffee Waste. *Sci. Rep.* **2020**, *10*, 2928. [CrossRef] [PubMed]
6. Ali, A.F.; Atwa, S.M.; El-Giar, E.M. Development of Magnetic Nanoparticles for Fluoride and Organic Matter Removal from Drinking Water. In *Water Purification*; Elsevier: Amsterdam, The Netherlands, 2017; pp. 209–262.
7. Jing, Y.; Li, L.; Zhang, Q.; Lu, P.; Liu, P.; Lü, X. Photocatalytic Ozonation of Dimethyl Phthalate with TiO_2 Prepared by a Hydrothermal Method. *J. Hazard. Mater.* **2011**, *189*, 40–47. [CrossRef]
8. Krishna, P.G.; Chandra Mishra, P.; Naika, M.M.; Gadewar, M.; Ananthaswamy, P.P.; Rao, S.; Boselin Prabhu, S.R.; Yatish, K.V.; Nagendra, H.G.; Moustafa, M.; et al. Photocatalytic Activity Induced by Metal Nanoparticles Synthesized by Sustainable Approaches: A Comprehensive Review. *Front. Chem.* **2022**, *10*, 917831. [CrossRef]
9. Luan, J.; Hou, P.-X.; Liu, C.; Shi, C.; Li, G.-X.; Cheng, H.-M. Efficient Adsorption of Organic Dyes on a Flexible Single-Wall Carbon Nanotube Film. *J. Mater. Chem. A* **2016**, *4*, 1191–1194. [CrossRef]
10. Papadakis, R. (Ed.) *Dyes and Pigments—Novel Applications and Wastewater Treatment*; IntechOpen: London, UK, 2021. [CrossRef]
11. Murugesan, A.; Loganathan, M.; Senthil Kumar, P.; Vo, D.-V.N. Cobalt and Nickel Oxides Supported Activated Carbon as an Effective Photocatalysts for the Degradation Methylene Blue Dye from Aquatic Environment. *Sustain. Chem. Pharm.* **2021**, *21*, 100406. [CrossRef]
12. Huang, P.; Kazlauciunas, A.; Menzel, R.; Lin, L. Determining the Mechanism and Efficiency of Industrial Dye Adsorption through Facile Structural Control of Organo-Montmorillonite Adsorbents. *ACS Appl. Mater. Interfaces* **2017**, *9*, 26383–26391. [CrossRef]
13. Gouthaman, A.; Azarudeen, R.S.; Gnanaprakasam, A.; Sivakumar, V.M.; Thirumarimurugan, M. Polymeric Nanocomposites for the Removal of Acid Red 52 Dye from Aqueous Solutions: Synthesis, Characterization, Kinetic and Isotherm Studies. *Ecotoxicol. Environ. Saf.* **2018**, *160*, 42–51. [CrossRef]
14. Wang, X.; Jiang, C.; Hou, B.; Wang, Y.; Hao, C.; Wu, J. Carbon Composite Lignin-Based Adsorbents for the Adsorption of Dyes. *Chemosphere* **2018**, *206*, 587–596. [CrossRef] [PubMed]
15. Naushad, M.; Ahamad, T.; AlOthman, Z.A.; Al-Muhtaseb, A.H. Green and Eco-Friendly Nanocomposite for the Removal of Toxic Hg(II) Metal Ion from Aqueous Environment: Adsorption Kinetics & Isotherm Modelling. *J. Mol. Liq.* **2019**, *279*, 1–8.
16. Zaidi, N.A.H.M.; Lim, L.B.L.; Usman, A.; Kooh, M.R.R. Efficient Adsorption of Malachite Green Dye using *Artocarpus odoratissimus* Leaves with Artificial Neural Network Modelling. *Desalination Water Treat.* **2018**, *101*, 313–324. [CrossRef]
17. Kooh, M.R.R.; Thotagamuge, R.; Chou Chau, Y.F.; Mahadi, A.H.; Lim, C.M. Machine Learning Approaches to Predict Adsorption Capacity of *Azolla pinnata* in the Removal of Methylene Blue. *J. Taiwan Inst. Chem. Eng.* **2022**, *132*, 104134. [CrossRef]
18. García-Padilla, Á.; Moreno-Sader, K.A.; Realpe, Á.; Acevedo-Morantes, M.; Soares, J.B.P. Evaluation of Adsorption Capacities of Nanocomposites Prepared from Bean Starch and Montmorillonite. *Sustain. Chem. Pharm.* **2020**, *17*, 100292. [CrossRef]
19. Pirsa, S.; Karimi Sani, I.; Khodayvandi, S. Design and Fabrication of Starch-Nano Clay Composite Films Loaded with Methyl Orange and Bromocresol Green for Determination of Spoilage in Milk Package. *Polym. Adv. Technol.* **2018**, *29*, 2750–2758. [CrossRef]
20. Abd El-Ghany, N.A.; Abu Elella, M.H.; Abdallah, H.M.; Mostafa, M.S.; Samy, M. Recent Advances in Various Starch Formulations for Wastewater Purification via Adsorption Technique: A Review. *J. Polym. Environ.* **2023**. [CrossRef]
21. Atta, A.M.; Al-Lohedan, H.A.; ALOthman, Z.A.; Abdel-Khalek, A.A.; Tawfeek, A.M. Characterization of Reactive Amphiphilic Montmorillonite Nanogels and Its Application for Removal of Toxic Cationic Dye and Heavy Metals Water Pollutants. *J. Ind. Eng. Chem.* **2015**, *31*, 374–384. [CrossRef]
22. Wilpiszewska, K.; Antosik, A.K.; Spychaj, T. Novel Hydrophilic Carboxymethyl Starch/Montmorillonite Nanocomposite Films. *Carbohydr. Polym.* **2015**, *128*, 82–89. [CrossRef]
23. Oleyaei, S.A.; Almasi, H.; Ghanbarzadeh, B.; Moayedi, A.A. Synergistic Reinforcing Effect of TiO_2 and Montmorillonite on Potato Starch Nanocomposite Films: Thermal, Mechanical and Barrier Properties. *Carbohydr. Polym.* **2016**, *152*, 253–262. [CrossRef] [PubMed]
24. Li, J.; Zhou, M.; Cheng, G.; Cheng, F.; Lin, Y.; Zhu, P.-X. Fabrication and Characterization of Starch-Based Nanocomposites Reinforced with Montmorillonite and Cellulose Nanofibers. *Carbohydr. Polym.* **2019**, *210*, 429–436. [CrossRef]
25. Zhu, J.; Zhang, S.; Pu, H.; Chen, X.; Zou, S.; Li, L.; Wang, Q. Structural Properties of Propionylated Starch-Based Nanocomposites Containing Different Amylose Contents. *Int. J. Biol. Macromol.* **2020**, *149*, 532–540. [CrossRef]
26. Haq, F.; Mehmood, S.; Haroon, M.; Kiran, M.; Waseem, K.; Aziz, T.; Farid, A. Role of Starch Based Materials as a Bio-sorbents for the Removal of Dyes and Heavy Metals from Wastewater. *J. Polym. Environ.* **2022**, *30*, 1730–1748. [CrossRef]

27. Chang, P.R.; Yu, J.; Ma, X. Preparation of Porous Starch and Its Use as a Structure-Directing Agent for Production of Porous Zinc Oxide. *Carbohydr. Polym.* **2011**, *83*, 1016–1019. [CrossRef]
28. Ma, X.; Liu, X.; Anderson, D.P.; Chang, P.R. Modification of Porous Starch for the Adsorption of Heavy Metal Ions from Aqueous Solution. *Food Chem.* **2015**, *181*, 133–139. [CrossRef]
29. Arroyo, M.; López-Manchado, M.A.; Herrero, B. Organo-Montmorillonite as Substitute of Carbon Black in Natural Rubber Compounds. *Polymer* **2003**, *44*, 2447–2453. [CrossRef]
30. Aouada, F.A.; Mattoso, L.H.C.; Longo, E. New Strategies in the Preparation of Exfoliated Thermoplastic Starch–Montmorillonite Nanocomposites. *Ind. Crop. Prod.* **2011**, *34*, 1502–1508. [CrossRef]
31. Yogananda, K.C.; Ramasamy, E.; Vasantha Kumar, S.; Rangappa, D. Synthesis, Characterization, and Dye-Sensitized Solar Cell Fabrication Using Potato Starch– and Potato Starch Nanocrystal–Based Gel Electrolytes. *Ionics* **2019**, *25*, 6035–6042. [CrossRef]
32. Ulbrich, M.; Asiri, S.A.; Bussert, R.; Flöter, E. Enzymatic Modification of Granular Potato Starch Using Isoamylase—Investigation of Morphological, Physicochemical, Molecular, and Techno-Functional Properties. *Starch-Stärke* **2021**, *73*, 2000080. [CrossRef]
33. Moreau, L.; Bindzus, W.; Hill, S. Influence of Salts on Starch Degradation: Part I—Sodium Chloride. *Starch-Stärke* **2011**, *63*, 669–675. [CrossRef]
34. Xu, E.; Wu, Z.; Long, J.; Jiao, A.; Jin, Z. Porous Starch-Based Material Prepared by Bioextrusion in the Presence of Zinc and Amylase–Magnesium Complex. *ACS Sustain. Chem. Eng.* **2018**, *6*, 9572–9578. [CrossRef]
35. Tetsuka, H.; Katayama, I.; Sakuma, H.; Tamura, K. Effects of Humidity and Interlayer Cations on the Frictional Strength of Montmorillonite. *Earth Planets Space* **2018**, *70*, 56. [CrossRef]
36. Sathyan, S.; Nisha, P. Optimization and Characterization of Porous Starch from Corn Starch and Application Studies in Emulsion Stabilization. *Food Bioprocess Technol.* **2022**, *15*, 2084–2099. [CrossRef]
37. Tian, H.; Wang, K.; Liu, D.; Yan, J.; Xiang, A.; Rajulu, A.V. Enhanced Mechanical and Thermal Properties of Poly (Vinyl Alcohol)/Corn Starch Blends by Nanoclay Intercalation. *Int. J. Biol. Macromol.* **2017**, *101*, 314–320. [CrossRef]
38. Sing, K.S.W. Reporting Physisorption Data for Gas/Solid Systems with Special Reference to the Determination of Surface Area and Porosity (Recommendations 1984). *Pure Appl. Chem.* **1985**, *57*, 603–619. [CrossRef]
39. Wang, F.; Chang, P.R.; Zheng, P.; Ma, X. Monolithic Porous Rectorite/Starch Composites: Fabrication, Modification and Adsorption. *Appl. Surf. Sci.* **2015**, *349*, 251–258. [CrossRef]
40. Naushad, M.; Ahamad, T.; Al-Maswari, B.M.; Abdullah Alqadami, A.; Alshehri, S.M. Nickel Ferrite Bearing Nitrogen-Doped Mesoporous Carbon as Efficient Adsorbent for the Removal of Highly Toxic Metal Ion from Aqueous Medium. *Chem. Eng. J.* **2017**, *330*, 1351–1360. [CrossRef]
41. Langmuir, I. The Adsorption of Gases on Plane Surfaces of Glass, Mica and Platinum. *J. Am. Chem. Soc.* **1918**, *40*, 1361–1403. [CrossRef]
42. Herbert, F. Over the Adsorption Solution. *J. Phys. Chem.* **1906**, *57*, 385–471.
43. Jalil, A.A.; Triwahyono, S.; Adam, S.H.; Rahim, N.D.; Aziz, M.A.A.; Hairom, N.H.H.; Razali, N.A.M.; Abidin, M.A.Z.; Mohamadiah, M.K.A. Adsorption of Methyl Orange from Aqueous Solution onto Calcined Lapindo Volcanic Mud. *J. Hazard. Mater.* **2010**, *181*, 755–762. [CrossRef]
44. Mohammadi, N.; Khani, H.; Gupta, V.K.; Amereh, E.; Agarwal, S. Adsorption Process of Methyl Orange Dye onto Mesoporous Carbon Material–Kinetic and Thermodynamic Studies. *J. Colloid Interface Sci.* **2011**, *362*, 457–462. [CrossRef]
45. Tanzifi, M.; Hosseini, S.H.; Kiadehi, A.D.; Olazar, M.; Karimipour, K.; Rezaiemehr, R.; Ali, I. Artificial Neural Network Optimization for Methyl Orange Adsorption onto Polyaniline Nano-Adsorbent: Kinetic, Isotherm and Thermodynamic Studies. *J. Mol. Liq.* **2017**, *244*, 189–200. [CrossRef]
46. Chen, J.; Shi, X.; Zhan, Y.; Qiu, X.; Du, Y.; Deng, H. Construction of Horizontal Stratum Landform-like Composite Foams and Their Methyl Orange Adsorption Capacity. *Appl. Surf. Sci.* **2017**, *397*, 133–143. [CrossRef]
47. Ai, Z.; Liu, C.; Zhang, Q.; Qu, J.; Li, Z.; He, X. Adding ZnO and SiO_2 to Scatter the Agglomeration of Mechanochemically Prepared Zn-Al LDH Precursor and Promote Its Adsorption toward Methyl Orange. *J. Alloys Compd.* **2018**, *763*, 342–348. [CrossRef]
48. Blaisi, N.I.; Zubair, M.; Ihsanullah; Ali, S.; Kazeem, T.S.; Manzar, M.S.; Al-Kutti, W.; Al Harthi, M.A. Date Palm Ash-MgAl-Layered Double Hydroxide Composite: Sustainable Adsorbent for Effective Removal of Methyl Orange and Eriochrome Black-T from Aqueous Phase. *Environ. Sci. Pollut. Res.* **2018**, *25*, 34319–34331. [CrossRef] [PubMed]
49. Satilmis, B.; Uyar, T. Amine Modified Electrospun PIM-1 Ultrafine Fibers for an Efficient Removal of Methyl Orange from an Aqueous System. *Appl. Surf. Sci.* **2018**, *453*, 220–229. [CrossRef]
50. Yönten, V.; Sanyürek, N.K.; Kivanç, M.R. A Thermodynamic and Kinetic Approach to Adsorption of Methyl Orange from Aqueous Solution Using a Low Cost Activated Carbon Prepared from *Vitis vinifera*, L. *Surf. Interfaces* **2020**, *20*, 100529. [CrossRef]
51. Ke, P.; Zeng, D.; Xu, K.; Cui, J.; Li, X.; Wang, G. Preparation of Quaternary Ammonium Salt-Modified Chitosan Microspheres and Their Application in Dyeing Wastewater Treatment. *ACS Omega* **2020**, *5*, 24700–24707. [CrossRef]
52. Omorogie, M.O.; Agbadaola, M.T.; Olatunde, A.M.; Helmreich, B.; Babalola, J.O. Surface Equilibrium and Dynamics for the Adsorption of Anionic Dyes onto MnO_2/Biomass Micro-Composite. *Green Chem. Lett. Rev.* **2022**, *15*, 51–60. [CrossRef]
53. Lagergren, S.; Sven, K. About the Theory of So-colled Adsorption of Soluble substances. *Handlingar* **1898**, *24*, 1–39.
54. Ho, Y.S.; McKay, G. Pseudo-Second Order Model for Sorption Processes. *Process Biochem.* **1999**, *34*, 451–465. [CrossRef]

55. Weber, W.J.; Morris, J.C. Kinetics of Adsorption on Carbon from Solution. *J. Sanit. Engrg. Div.* **1963**, *89*, 31–59. [CrossRef]
56. Jawad, A.H.; Mamat, N.F.H.; Hameed, B.H.; Ismail, K. Biofilm of Cross-Linked Chitosan-Ethylene Glycol Diglycidyl Ether for Removal of Reactive Red 120 and Methyl Orange: Adsorption and Mechanism Studies. *J. Environ. Chem. Eng.* **2019**, *7*, 102965. [CrossRef]